Transferable tight-binding description of the Fe-C interaction

Article · February 2012

3 authors, including:

Nicholas Hatcher
QuesTek Innovations LLC, Evanston, IL USA
16 PUBLICATIONS   **223** CITATIONS

SEE PROFILE

Georg K. H. Madsen
Interdisciplinary Centre for Advanced Materials Simulation
147 PUBLICATIONS   **18,630** CITATIONS

SEE PROFILE

Some of the authors of this publication are also working on these related projects:

Thermal Conductivity calcualtions View project

Monochalcogenides View project

DFT-based tight-binding modeling of iron-carbon

Nicholas Hatcher, Georg K. H. Madsen, and Ralf Drautz

ICAMS, Ruhr-Universität Bochum, 44780 Bochum, Germany

A coherent transferable tight-binding (TB) parametrization including magnetism has been developed for the Fe-C interaction. We use a downfolding procedure to obtain continuous and transferable Fe-C bond integrals from density functional theory. A TB model is constructed using these bond integrals and a parameterized interatomic repulsion based on simple exponentials fit to the excess energy of interstitial carbon in α, γ, and ϵ iron. An accurate description of the energy hierarchy of these structures can be achieved with only three fitting parameters. The model is used to calculate bulk properties and energies of a variety of Fe carbides, and good agreement is found for a number of properties. Excellent agreement with the individual elastic constants of cementite is achieved. We obtain a satisfactory migration energy barrier of carbon in α iron and confirm the instability of carbon in the tetrahedral interstitial site. Defect binding energies are calculated for a number of defects and largely agree with density functional theory calculations. This simple model based on physical insights may be used to study systems containing thousands of atoms. Furthermore, it may be employed as the basis for $O(N)$ bond-order potentials.

PACS number(s): 71.20.Be, 75.50.Bb, 61.72.J−

I. INTRODUCTION

Despite the technological importance of steel, the description of the complex structural, elastic, electronic, and thermodynamic processes that provide steel with its exceptional properties is incomplete. As carbon affects steel at very low concentrations, fundamental advancements in modeling the iron-carbon interaction can clarify mechanisms governing steel properties. To this end density functional theory (DFT) calculations have been employed to calculate the interaction of carbon with iron. These include the minimum-energy path (MEP) of interstitial carbon in austenite and ferrite,[1] the binding energy of carbon and vacancy defects in α iron,[2,3] magnetic ordering during diffusion,[4,5] and the excess enthalpy of carbon in ferrite under stress.[6] The influence and interactions among carbides in steel further determine its attributes. DFT studies of cementite, the most prevalent carbide in steel, have examined elasticity,[7] thermodynamic stability including formation energies,[8] and vibrational, electronic, and magnetic contributions to entropy.[9] This research provides *ab initio* thermodynamic parameters for phase diagram prediction methods such as CALPHAD. Additional carbides, including Fe_5C_2, Fe_2C, $Fe_{23}C_6$, and Fe_7C_3, have also been studied in order to understand their electronic structures and relative stabilities.[10–14]

While DFT calculations have given relatively accurate results, their applicability has been limited to periodic systems containing less than a few hundred atoms. Interatomic potentials, such as embedded atom models (EAMs),[15] provide a link from atomistic simulations to microstructural models (e.g., continuum and finite element-based methods). EAMs use a function based on the charge density of the surrounding atoms, and a number of EAM potentials have been developed for the iron-carbon interaction. These methods have shown successes including the ability to calculate the formation energies and configurations of defects, multicarbon, and vacancy clusters;[16] MEPs for carbon diffusion in ferrite and screw dislocations;[3] accurate carbon-carbon interactions and the core structure of screw dislocation within iron via DFT-based potentials;[17] and even dynamics of the ferrite-cementite interface.[18] Despite these modeling achievements, a recent study by Hristova *et al.* showed that a simple homogeneous volume change applied to each of these models revealed inconsistencies with DFT.[6] Each EAM potential behaved strikingly different when the excess enthalpy was calculated as a fraction of volume change. A further handicap to EAM potentials is their inability to be utilized for structures for which they were not fitted, for example, cementite or austenitic (fcc) iron. Thus, there is a clear need for methods which incorporate interatomic bonding and are transferable to a range of configurations, yet are simple enough to be employed for systems containing thousands of atoms. Additionally, a model with the intrinsic treatment of magnetism is required for steel calculations.

Tight-binding (TB) methods provide the requisite elements for bridging electronic structure calculations to microscopic modeling. TB is a second-order approximation of DFT, but uses a parametrization of the interatomic interaction, thereby enabling it to treat thousands of atoms. These methods form the basis of the $O(N)$ bond-order potentials (BOPs),[19–21] which coarse grain the electronic structure for the treatment of millions of atoms. Furthermore, magnetism may be directly treated within the energy functional.[22] The creation of TB methods for Ni and Ti carbides has been displayed in Refs. 23 and 24.

We choose an orthogonal *pd* model as it is both simple and accounts for the main bonding in the system. Our TB model is constructed with a bonding term extracted directly from DFT calculations via a simple parametrization of the resulting bond integrals. This has been previously applied for metals including iron, manganese, and chromium with extensions to binary alloys.[25,26] The iron-carbon model described here uses the Fe-Fe TB model described previously[25] and the methodology thus provides a both coherent and systematic approach to multicomponent systems. Given the focus on steel, C-C interactions are described within the dilute limit in steel and carbides. The present model will give qualitatively correct energies, electronic structures, and magnetic properties for a range of compositions from carbides to pure iron.

This paper will proceed as follows. First, our TB model will be explained in Sec. II. In Sec. II A the procedure for obtaining our bonding energy is elucidated. To affirm the efficacy of the extraction of DFT bond integrals, TB and DFT densities of states for Fe-C structures are compared and give good agreement. Fitting is performed in Sec. II B on the excess energies of interstitial carbon in iron for repulsive terms of the TB model, and we obtain energies comparable to DFT. Due to carbon's affinity for forming dimers, modifications to the carbon model are explained in Sec. II C.

In Sec. III we apply the model to test the stability of carbides and energies of various carbon defects. We first look at formation and migration energies of single carbon atoms in α, γ, and ϵ iron in Sec. III A. Next, we examine carbides and find that our TB model gives the correct quantitative and qualitative results for the lattice constants, energies, and bulk modulus of cementite and a number of other structures. These findings and elastic constants of cementite are explained in Sec. III B. Finally, in Sec. III C the binding energies of a range of vacancies and defects are calculated and compared with experiment and DFT calculations.

Conclusions and future prospective uses for this model are given in Sec. IV.

II. METHOD

As used earlier[25,26] the total energy function is based on an orthogonal TB method assuming local charge neutrality[27] and is given as

$$E_{TB} = E_{\text{bond}} + E_{\text{mag}} + E_{\text{rep}} + E_{\text{emb}} - E_{\text{free atoms}}. \quad (1)$$

Bonding is captured by the density matrix times a simplified Hamiltonian as

$$E_{\text{bond}} = \sum_{\sigma=\uparrow,\downarrow} \sum_{I\mu J\nu, I\neq J} \rho^{\sigma}_{I\mu J\nu} H_{J\nu I\mu}, \quad (2)$$

where I and J label the atoms in the system, μ and ν the basis functions, and σ the spin. The Hamiltonian is modeled using orthogonal pd two-center model which is explained in the following section. Since there is only one orbital type per atom, promotion terms are not required. Magnetism is
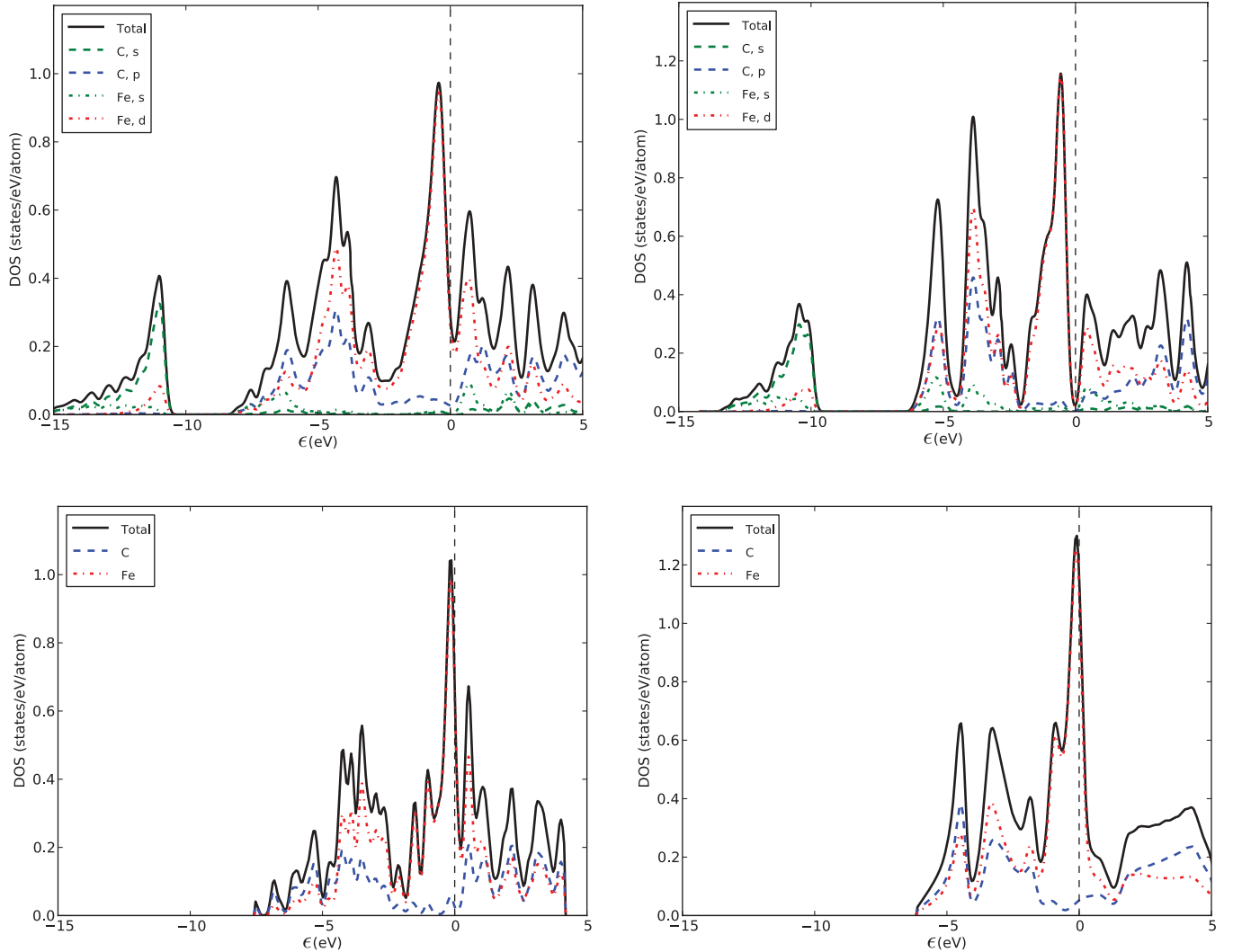

FIG. 1. (Color online) DFT (top panels) vs TB (bottom panels) DOS for B1 FeC (prototype NaCl) (left panels) and B3 FeC (prototype Zn-blende) (right panels).
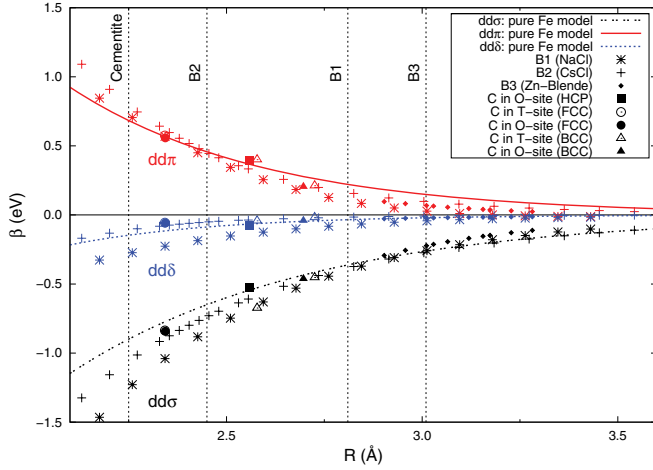
FIG. 2. (Color online) Bond integrals for the Fe-Fe interaction in Fe-C structures. The pure Fe-model is taken from Ref. 25. Vertical lines denote equilibrium interatomic distances of the nearest Fe-Fe neighbors. Structures include iron with carbon placed in the octahedral (O) and tetrahedral (T) interstitial sites.

calculated within the Stoner model as

$$E_{\mathrm{mag}} = -\frac{1}{4}\sum_J I_J m_J^2,\tag{3}$$

where m_J is the magnetic moment and I_J is the Stoner parameter on atom J. I_J is set to zero for carbon, as explained in Sec. II A, and for iron we use an I_J of 0.76, as inherited from Ref. 25. The repulsion is modeled as a pairwise repulsive term,

$$E_{\mathrm{rep}} = \sum_{I,J\neq I} a_{\mathrm{rep}}^{IJ} e^{-b_{\mathrm{rep}}^{IJ} R_{IJ}},\tag{4}$$

and for iron balanced with an attractive Finnis-Sinclair type embedding potential, E_{emb}, that models the largely volume-dependent contribution of the s electron to bond formation,

$$E_{\mathrm{emb}} = \sum_I \left[\sum_{J\neq I} \left(a_{\mathrm{emb}}^{IJ}\right)^2 e^{-b_{\mathrm{emb}}^{IJ} R_{IJ}^2} \right]^n,\tag{5}$$

where a_{rep}^{IJ}, b_{rep}^{IJ}, a_{emb}^{IJ}, b_{emb}^{IJ}, and n are parameters which will be explained in Sec. II B and R_{IJ} is the interatomic distance. We find that the Fe-C and C-C interactions do not require an embedding potential despite its continued use in the

inherited Fe-Fe model. Last, we subtract the DFT energy of the nonmagnetic free atoms.

A. Hamiltonian model

We obtain the two-center Slater-Koster (SK) integrals[28] from a downfolding procedure described earlier.[25] The scheme takes advantage of the dual grid and atomic basis implemented in the code GPAW[29,30] and downfolds an extended multiple-ζ basis set onto a minimal basis set.[25] For a particular structure an optimal minimal basis is established from which the interatomic bond integrals are calculated. As these bond integrals have been shown to be initially discontinuous for different structures, we find that by performing a Löwdin orthogonalization continuity is restored and environmental dependence is effectively screened while capturing two-center interactions.[25] Other authors have investigated similar schemes.[31] We choose to develop a pd valent model both for simplicity and because it is found by examining the DFT densities of states (DOS) for Fe-C structures that the carbon s states are reasonably separated from the primarily pd dominated band near the Fermi level (see Fig. 1).

The Fe-Fe dd bond integrals for both carbon-rich and dilute test cases have been calculated and are shown in Fig. 2. The values show a good agreement with the results obtained previously for pure Fe (Ref. 25). A similar transferability of the SK bond integrals was observed for the alloys of Cr, Mn, and Fe (Ref. 26), confirming that it is possible to build a coherent and systematic library of two-center interactions. We will thus build our model on the previous short-ranged Fe-Fe model[25] and only develop parametrizations of the Fe-C and C-C interaction. The Fe-Fe parameters are given in Table I.

In the minimal basis SK two-center approximation of the Fe-C Hamiltonian, only the $ss\sigma$, $sp\sigma$, $ds\sigma$, $dp\sigma$, and $dp\pi$ bond integrals are nonzero by symmetry. In our orthogonal pd valent model we retain only the $dp\sigma$ and $dp\pi$ bond integrals. The orthogonalized bond integrals for the iron-carbon interaction are shown in Fig. 3. The bonding terms fall on the same line throughout a wide range of interatomic distances and environments. This holds for a variety of structures including the ordered B1 (NaCl), B2 (CsCl), and B3 (Zn-Blende) structures; cementite; and carbon in the octahedral and tetrahedral sites of bcc, fcc, and hcp iron. Each of these bond integrals matches that of the pure two-center compound, the Fe-C dimer, despite a deviation at distances under 1.75 Å. Regarding this deviation, the DOS of cementite

TABLE I. TB model parameters. The Fe-Fe parameters are taken from Ref. 25. The C-C bonding interaction is cut off at short distances (see Sec. II C).

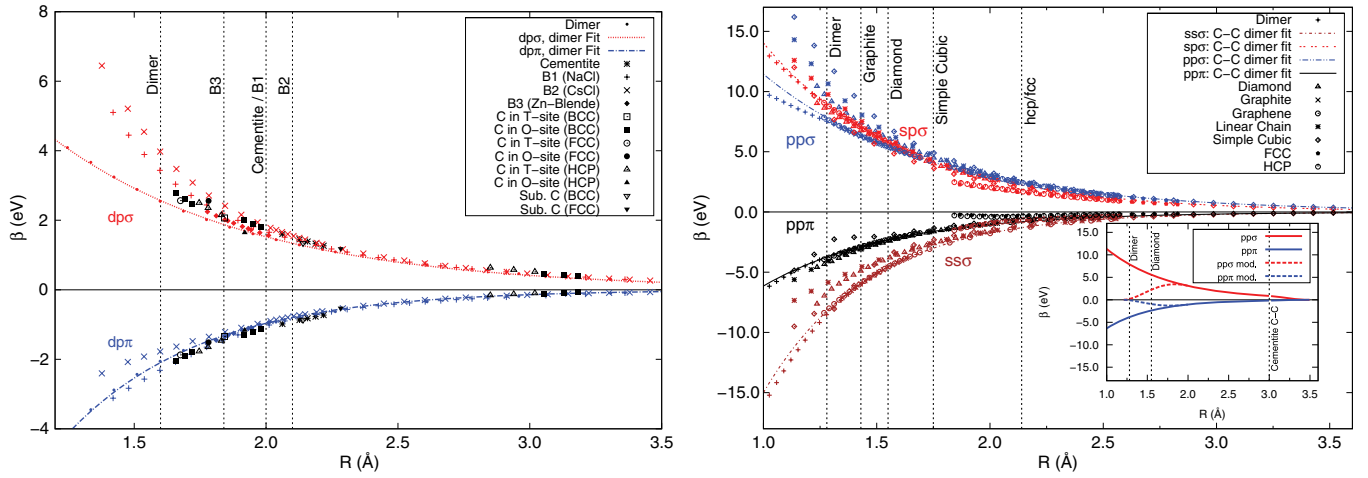| Bonding	a (eV)	b (Å^{-1})	Repulsive	a (eV)	b (Å^{-1})
Fe-Fe $dd\sigma$	-34.811	1.625	Fe-Fe E_{rep}	1031.00	3.25
Fe-Fe $dd\pi$	63.512	2.014	Fe-Fe E_{emb}	3.69	0.23
Fe-Fe $dd\delta$	-50.625	2.597			
Fe-C $dp\sigma$	20.611	1.302	Fe-C E_{rep}	11718.85	5.217
Fe-C $dp\pi$	-46.371	1.936			
C-C $pp\sigma$	44.538	1.359	C-C E_{rep}	220.67	2.586
C-C $pp\pi$	-36.574	1.783			
d_{cut}, R_{cut} (Å)	0.5	3.5	d_{cut}, R_{cut} (Å)	0.5	5.5

FIG. 3. (Color online) Bond integrals for the Fe-C (left) and the C-C interaction (right). The equilibrium nearest-neighbor interatomic distances for each structure are marked by vertical lines. For the Fe-C interaction, carbon is placed in octahedral (O), tetrahedral (T), and substitutional (Sub.) sites in bcc, fcc, and hcp iron.

was calculated using both a fit to the dimer and one fit to the B1 structure and no significant deviations were found between the two DOS results. Thus, we parametrize the $dp\sigma$ and $dp\pi$ bonding integrals as simple exponentials (see Fig. 3 and Table I).

A cutoff function, taken in the form of a cosine damping function,[25] is applied to all bond integrals to restrict the number of neighbors involved in setting up the Hamiltonian (see Table I for the cutoff radius). This same cutoff function will be employed for cutoffs to the repulsive interactions.

For the carbon-carbon interaction, we use the same downfolding procedure and obtain bond integrals from DFT for the $ss\sigma$, $sp\sigma$, $pp\sigma$, and $pp\pi$ states for a range of structures [see Fig. 3 (right)]. These results may be fitted with a simple exponential despite small deviations from this fit due to hcp and fcc carbon, which likely arises from the close-packing nature of these structures. We incorporate the $pp\sigma$ and $pp\pi$ carbon-carbon bond integrals into our TB model, in Table I, also using a fit to the dimer interactions.

In the TB calculations the Stoner parameter is taken to be zero for carbon and 0.76 eV for iron (as taken from Ref. 25). The iron Stoner parameter was shown to yield a magnetic moment enhancement of around 0.4 μ_B/atom. For carbon, while Stoner parameter values as high as 2.3 eV have been suggested,[32] we find that the magnetic moment on interstitial carbon atoms in α iron is already overestimated by around 0.1 μ_B/atom with a parameter of zero. This rises to 0.3 μ_B/atom when the parameter is increased to the published 2.3-eV value. Thus, we set I_{carbon} to zero.

Omitting the s electrons means that the number of electrons must be introduced as a parameter. The parameter can be obtained from the density matrix of the minimal basis DFT calculation. Doing this we obtain $N_p \approx 3$ for carbon and $N_d \approx 7$ for iron. We fix $N_p = 3.0$ and $N_d = 6.8$, as used earlier for pure iron[25] and calculate the on-site levels self-consistently by assuming local charge neutrality.

The resulting DOS of FeC in the B1 and B3 structures, which have octahedral and tetrahedral coordination, respectively, are shown in Fig. 1. Peak positions and bandwidth agree

well between the DOS of DFT and TB model. The TB model gives higher peaks and a slightly smaller bandwidth, due to the minimal basis and the lack of iron s states at the bottom of the main band. However, the number, location, and relative heights of carbon-p and iron-d states are similar. Thus, major features are replicated in this coarse-grained description. The lack of an s band below -10 eV arises due to the omission of s states in our pd valent model. As it is well separated from the main band, this should not greatly affect bonding or properties calculations.

In Fig. 4 the DOS for ferromagnetic cementite and carbon in the octahedral interstitial of bcc Fe are shown. A similar agreement, albeit with condensed band widths and enhanced peaks, as was found for nonmagnetic calculations is observed. Again, there is good agreement among the overall shape of the primary band, the location of the Fermi energy, and the individual relative peak locations in the band. The relative shift of the spin-up and spin-down states agrees well with DFT results, giving a comparable magnetic moment. Thus, we are able to obtain bonding interactions in a number of Fe-C structures which agree with DFT.

The agreement between DFT and TB DOS, observed for both magnetic and nonmagnetic structures, justifies the omission of the iron and carbon s states in our model. This is supported by results of the magnetic moments of cementite and carbon in an octahedral interstitial of a $2 \times 2 \times 2$ α-iron supercell. The calculated magnetic moment for iron in cementite was 2.08 μ_B versus 1.86 μ_B in DFT [Vienna *ab initio* simulation package (VASP)], while the magnetic moment of iron in the supercell was 2.42 μ_B versus 2.06 μ_B in DFT (present calculations). While there is some enhancement of magnetism in our TB model (as found in the Fe model of Ref. 25), we obtain both qualitative and quantitative agreement in the magnetic properties for these disparate structures.

B. Repulsive Fe-C terms

As the bonding terms are fully attractive, a repulsive term is required to balance atomic attraction [see Eq. (4)]. Two fitting
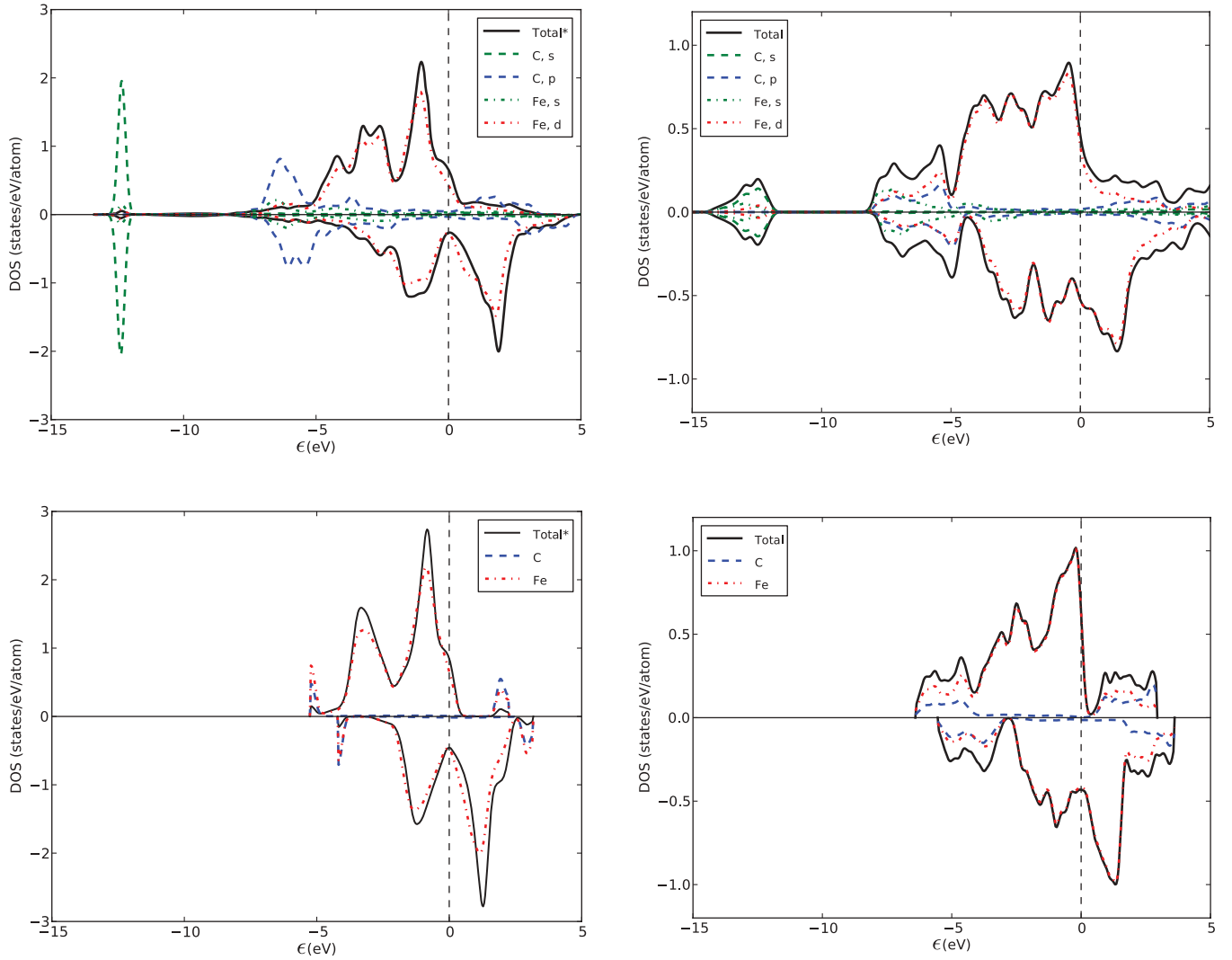
FIG. 4. (Color online) DFT (top panels) vs TB (bottom panels) DOS of a carbon atom in the octahedral interstitial site of a relaxed spin-polarized $3 \times 3 \times 3$ cell of bcc iron (left panels) and cementite (right panels). For bcc iron total DOS represents the average DOS per atom, while the projected DOS represents the DOS for the carbon atom and its six nearest neighbors.

parameters remain in our repulsive equation, a_{rep}^{FeC} and b_{rep}^{FeC}. To isolate the Fe-C interaction, we perform a least-squares fitting of the excess energy of carbon in bcc, fcc, and hcp iron in both the octahedral (O) and tetrahedral (T) interstitial sites using relaxed structures of the iron supercell with a carbon interstitial. Supercells of $2 \times 2 \times 2$ conventional cells were chosen: 32 iron atoms in fcc and 16 in bcc and hcp. Tests were then performed on much larger cells (see the following section) and compared with current and previous DFT calculations to ensure this model would perform well in the dilute limit. By focusing on the excess energy, iron-iron interactions and the carbon binding energy are effectively canceled and we fit the remaining Fe-C interactions.

C. Repulsive C-C terms

To complete our TB model in instances when carbon atoms interact, we must also add a repulsive term between carbon atoms. Therefore, we choose to fit the carbon-carbon repulsion

to cementite, as this is the most prevalent carbide occurring in steel. The repulsive energy is taken as proportional to the overlap repulsion of the atoms, so for b_{rep}^{IJ} we take the square of the longest ranged term in the C-C interaction, $pp\sigma$, which yields an exponential $\exp(-2.586\text{Å}^{-1} \cdot R)$. The other parameter, a_{rep}^{CC}, is then fit to cementite, and we obtain a value of 220.67 eV. A number of other carbides are examined in Sec. III B. See Table I for a list of our repulsive parameters.

Due to the omission of s states and since the C-C repulsion was fit to cementite, the carbon model initially incorrectly stabilizes the carbon dimer as found in other TB models.[24] This arises from the inability to replicate hybridized sp^2 and sp^3 bonding of the graphite and diamond, respectively, in a pure p model with no s states. To correct this problem without affecting cementite or other carbide structures, we apply a short-range modification to the bond integrals effectively reducing the bonding to zero with the bond distance [see $pp\sigma$-mod. and $pp\pi$-mod. in Fig. 3 (right)]. This short-range

term is general and applied to all carbon interactions. As such, it is easy to implement in a TB framework. The modification is achieved by a cosine damping function employed in the opposite direction as used for the exponential cutoff, starting at 2.0 Å and reducing the bond integrals to zero at 1.2 Å.

An alternative to this short-range cutoff is to add an attractive embedding term [i.e., Eq. (5)] to the exponential repulsion obtained from fitting cementite. This would lower the energies of the carbon-only structures giving better agreement with DFT. To destabilize the carbon dimer a hard-core repulsive term would be required. We find, however, that this creates a number of nodes in the TB energies of carbon-only structures when varied over a large range of lattice constants. While giving better binding energy agreement with DFT, this alternative model would generate difficulties by creating metastable fcc and hcp states as well as causing discontinuities in the derivative of the energy versus lattice constant.

This quite simple model for carbon gives the correct qualitative ordering of the phases (with the exception of the simple cubic stabilized with respect to the linear chain) and the correct ordering of the lattice constants (see Fig. 5) as found by DFT. Because we use nonmagnetic free carbon atoms as the reference state, the DFT data given in Fig. 5 needs to be shifted up by the magnetic energy of the free atoms (more than one electron volt per atom) for the calculation of the binding energy. Still, even if this shift is taken into account, the present TB model predicts binding energies that are too low in magnitude and equilibrium lattice constants that are around 0.5 Å too large. This limits the model's ability to correctly calculate total energies for carbon-only structures in iron. As we develop this model for Fe-rich structures, pure carbon is outside the scope of the present work. We further lower the binding energy of carbon structures compared to Fig. 5 by adding a constant energy offset to the free carbon atoms. The energy offset is chosen such that the formation energy of cementite in DFT and TB agree. Furthermore, as the C-C nearest-neighbor distances in cementite are approximately 3 Å, the bonding cutoff does not influence cementite or other iron-rich carbides.

III. RESULTS

To test this model, we compare a number of TB calculated properties with DFT. In order to ensure that the TB model is applicable across a range of DFT implementations, and to allow direct comparisons with many results currently available in the literature, we use the VASP[33–35] within the projector-augmented wave (PAW) method.[36,37] The GGA-PBE exchange correlation functional was employed. Energy convergence was achieved for most structures with a plane-wave cutoff set to 500 eV and a k-point mesh of 6000 k points divided by the number of atoms in the reciprocal cell. A similar k-point mesh was used for TB calculations, which gave a convergence for the various structures of around 2 meV/atom.

In this section, we first examine the energies and behavior of an isolated carbon in iron in Sec. III A. Then, in Sec. III B we examine the structural stability of a variety of Fe carbides including elastic properties. Finally, in Sec. III C we compare DFT and TB defect and defect-pair energies.

A. Isolated carbon in iron

To discuss the energetics of carbon solution in iron, the energy of carbon in iron is compared to graphite and α iron as

$$E^{\text{exc}}(V) = E_{\text{Fe}_N\text{C}}(V) - \left(N \cdot E_{\text{Fe}}^{\text{FM-bcc}}(V) + E_{\text{C}}^{\text{graphite}}(V_0) \right),$$
(6)

where $E_{\text{Fe}_N\text{C}}$ is the total energy of the supercell and $E_{\text{Fe}}^{\text{FM-bcc}}$ and $E_{\text{C}}^{\text{graphite}}$ are the per-atom binding energies.

The energy differences between O and T carbon occupations are within tens (for hcp) to a few hundreds (for bcc and fcc) of meV to DFT as shown in Fig. 6 and quantified in Table III. Importantly, the slope of the change in energy with increasing volume is in very good agreement with DFT for both O and T sites in all structures (see Fig. 6). As the fitting was performed for relaxed structures, nonrelaxed structures do not have the same degree of quantitative agreement, but they still exhibit qualitative agreement and correct ordering. As shown in Table II, the present TB calculations obtain the correct energy of O-carbon in bcc within 100 meV of present
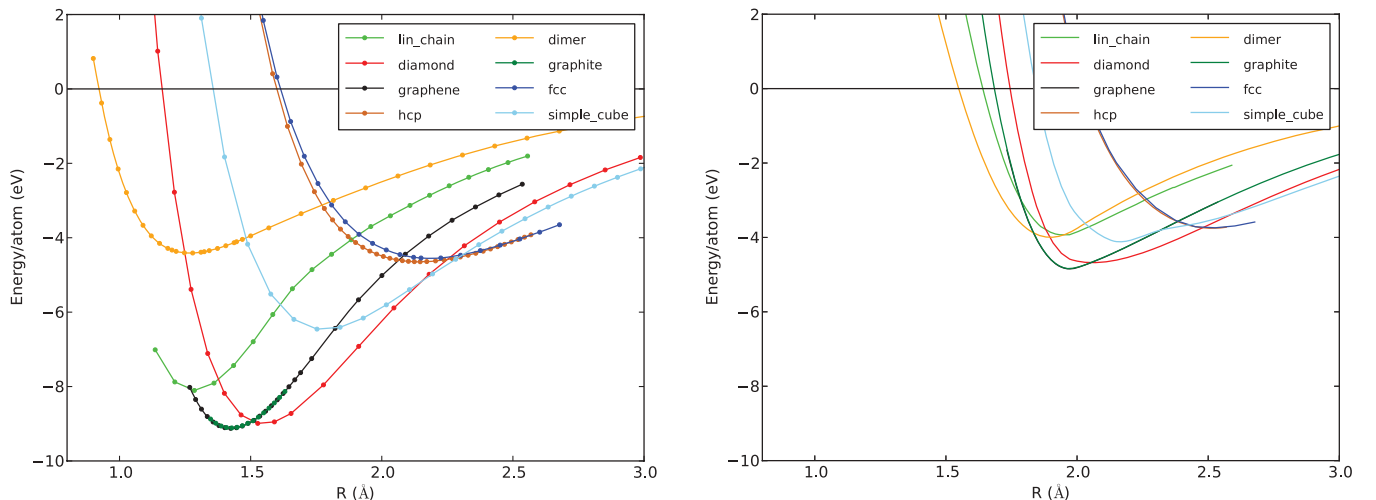

FIG. 5. (Color online) Binding energies of carbon structures from DFT (left) and the present TB method (right).
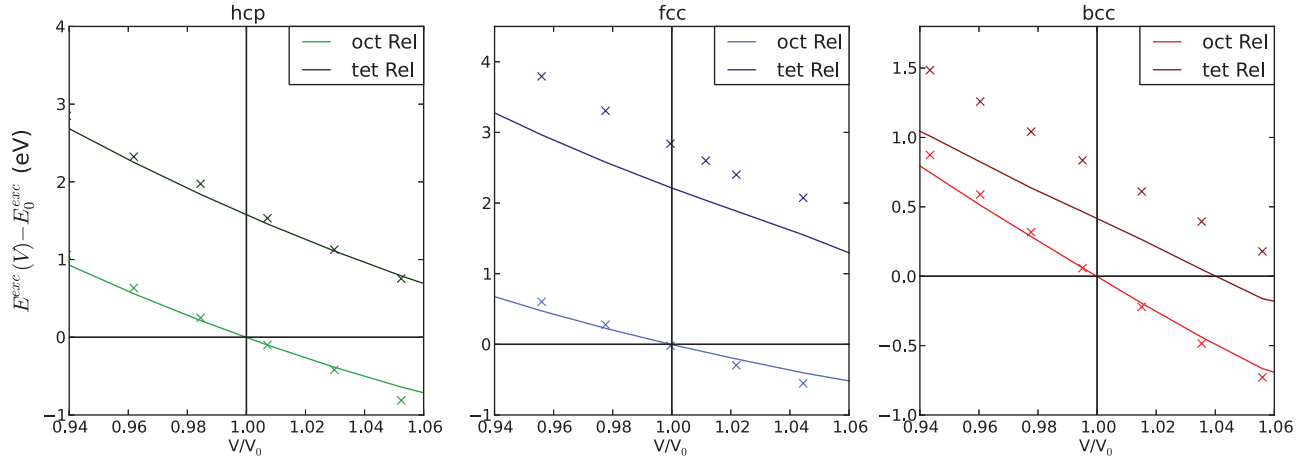
FIG. 6. (Color online) Excess energies of fcc bcc and hcp iron with carbon in the octahedral and tetrahedral interstitial sites of $2 \times 2 \times 2$ supercells. DFT results are represented by $\times$'s, whereas TB results are given as lines. V_0 refers to the undistorted Fe-only unit cell of bcc, fcc, and hcp-iron. The energies of both TB and DFT calculations are shifted so that the energy of carbon in the octahedral interstitial position at V_0 is zero. See Table II for the original data.

and previous DFT calculations for $Fe_{16}C$, $Fe_{54}C$, and $Fe_{128}C$. For O-carbon in fcc and hcp, calculated using NM structures, the TB model gives lower excess energy values than the present GPAW calculations. However, previous DFT excess energies for fcc using the high-spin fcc state agree more closely with the

present TB calculations and show the same trends that excess energy lowers as system size is increased. The bcc results are in much better agreement with DFT than other EAM results, and the relaxed volume is reproduced as well. Furthermore, as shown by Hristova *et al.* using a $3 \times 3 \times 3$ supercell of

TABLE II. Calculated TB excess energies of carbon in iron in comparison with DFT and experiment (see Sec. III A for additional details). Volumes and atomic positions have been relaxed.

	Method	Cell	Volume ($\mathring{A}^3$/Fe atom)	E^{exc} (eV)
bcc	DFT[a]	$Fe_{54}C$	11.42	0.72
	DFT[b]	$Fe_{128}C$	11.70	0.74
	MEAM[c]	$Fe_{54}C$	11.74	1.28
	EAM[d]	$Fe_{54}C$	11.78	-7.04
	EAM[e]	$Fe_{54}C$	11.68	1.81
	EAM[f]	$Fe_{54}C$	11.64	-6.26
	DFT[g]	$Fe_{16}C$	12.22	1.03
	TB[h]	$Fe_{16}C$	12.37	1.09
	TB[h]	$Fe_{54}C$	11.73	0.85
	TB[h]	$Fe_{128}C$	11.59	0.82
	Expt.[i]			0.6–0.78, 0.9–1.3
fcc	DFT[b]	$Fe_{32}C$	12.29	-0.06
	DFT[b]	$Fe_{125}C$	12.06	-0.17
	DFT[g]	$Fe_{32}C$	10.58	0.26
	TB[h]	$Fe_{32}C$	10.56	-0.19
	TB[h]	$Fe_{108}C$	10.45	-0.26
hcp	DFT[g]	$Fe_{16}C$	10.82	1.15
	TB[h]	$Fe_{16}C$	10.78	0.45
	TB[h]	$Fe_{128}C$	10.41	0.25

[a]VASP calculation from Ref. 6.
[b]VASP calculation from Ref. 1 (high-spin fcc).
[c]MEAM calculation from Ref. 6.
[d]Lau EAM calculation from Ref. 6.
[e]Ruda EAM calculation from Ref. 6.
[f]Hepburn EAM calculation from Ref. 6 fit to -6.27.
[g]Present GPAW calculations (NM fcc).
[h]Present model (NM fcc).
[i]Experiments outlined in Ref. 6.

TABLE III. Calculated TB migration energies for relaxed structures calculated as the differences between the energies of octahedral and tetrahedral carbon interstitial occupations in comparison with DFT and experiment.

	Method	Cell	Energy (eV)
bcc	DFT[a]	$Fe_{128}C_1$	0.86
	DFT[b]	$Fe_{128}C_1$	0.90
	EAM[c]	$Fe_{128}C_1$	0.85
	TB[d]	$Fe_{128}C_1$	0.70
	Expts.[e]	bcc	0.81–0.88
fcc	DFT[f]	$Fe_{32}C_1$	2.70
	TB[d]	$Fe_{32}C_1$	2.09
	TB[d]	$Fe_{256}C_1$	1.74
hcp	DFT[f]	$Fe_{16}C_1$	1.50
	TB[d]	$Fe_{16}C_1$	1.44
	TB[d]	$Fe_{256}C_1$	1.15

[a]VASP calculation from Ref. 1.
[b]VASP calculation from Ref. 3.
[c]EAM calculation from Ref. 3.
[d]Present model.
[e]See text for details.
[f]GPAW calculations.

54 atoms,[6] the E^{exc} slope during a simple volume distortion of our present TB method is in better agreement with DFT than any of these EAM methods (see Fig. 7).

It has been established that interstitial carbon will occupy the octahedral hole of α iron and that there is no local minimum in the diffusion path between adjoining octahedral sites.[1–3] To confirm that our model reproduces this behavior we performed nudged elastic band (NEB) calculations moving carbon from the tetrahedral to octahedral interstitial sites. This
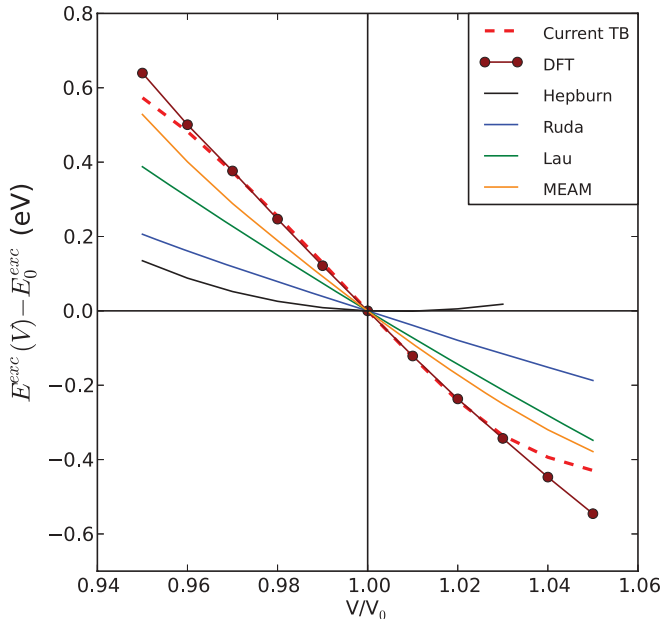

FIG. 7. (Color online) Excess energies of octahedral interstitial carbon in a $3 \times 3 \times 3$ supercell of bcc FM iron in comparison with previous DFT and EAM results (see Ref. 6 for EAM and DFT details). V_0 refers to the undistorted Fe-only unit cell.
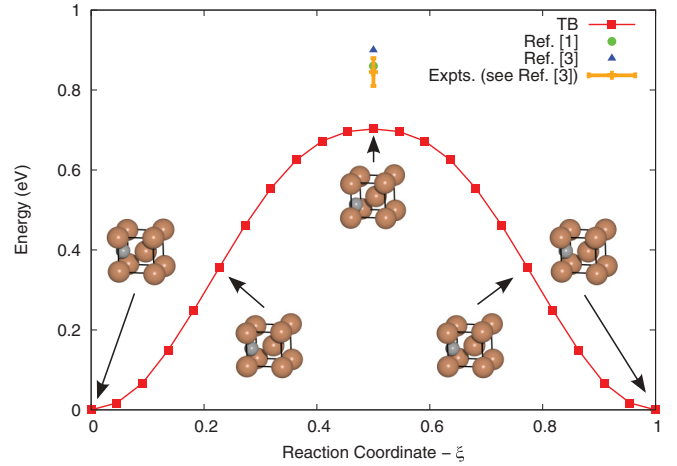

FIG. 8. (Color online) Migration energy barrier for carbon in α iron. Carbon begins in the stable octahedral interstitial site, proceeds to the unstable tetrahedral interstitial site ($\xi = 0.5$), and then continues to a new octahedral interstitial site at $\xi = 1.0$.

was performed in a 54 iron-atom unit cell with one carbon, and we obtained a migration energy barrier of 0.70 eV (see Fig. 8 and Table III). We used a fine sampling of ten images between the tetrahedral and octahedral starting and ending points and found no minima on the NEB path. Thus, carbon in the tetrahedral site of α iron is unstable in our TB model. This value compares with 0.90 eV calculated in Ref. 3 and 0.86 eV calculated in Ref. 1. Experiments compiled in Ref. 3 have shown a range of 0.81–0.88 eV.

The relaxation of carbon in α iron is an important quantity for testing the ability to use this model for relaxing complex interfaces or performing molecular dynamics simulations. Thus, we calculate the relaxation of iron atoms surrounding a carbon atom in the tetrahedral and octahedral site and compare it with previous DFT calculations.[2] For the octahedrally coordinated carbon, we obtained an iron nearest-neighbor relaxation of 35% versus a literature value of 24%; for tetrahedrally coordinated carbon, our model predicts a 23% relaxation versus 14% in DFT. Thus, our model overestimates the carbon-iron repulsion causing over-relaxation of the iron atoms away from carbon.

B. Structural stability of carbides

We obtain the energies of formation, bulk modulus, and lattice constants of a number of carbide structures. We list these properties in Table IV as compared with DFT. We achieve the correct energetic ordering of the simple carbides and cementite. Lattice constants are in good agreement with volume deviations of less than 5% for all carbides. Formation energies also largely have the correct ordering. TB carbides are destabilized with respect to cementite (prototype Fe_3C) as compared to DFT calculations, suggesting that no carbide phases inadvertently stabilize in MD or optimization simulations. VASP calculations show that the DFT energy of "upper bainite" (prototype Fe_3N, the regular $P6_322$ structure) is only 1 meV/atom above the DFT energy of cementite. In addition, several other structures including Fe_2C, Fe_7C_3, $Fe_{23}C_6$, and Fe_5C_2 are within a few meVs/atom of cementite. In contrast,

TABLE IV. Calculated TB model results vs DFT of carbide structures. E_f is the formation energy per atom, $E_f = E_{Fe_xC_{1-x}} - (x \cdot E_{Fe}^{bcc} + (1-x) \cdot E_C^{graphite})$. The magnetic moment (where applicable) is the moment per iron atom. All DFT calculations are from the present work.

	V (Å^3/atom)		E_f		B_0 (GPa)		μ	
	TB	DFT	TB	DFT	TB	DFT	TB	DFT
Fe$_3$C	9.24	9.50	0.045	0.045	232	225	2.07	1.86
Fe$_3$N	10.12	10.15	0.160	0.046	252	203	2.20	1.97
Fe$_{23}$C$_6$	9.56	9.94	0.087	0.041	189	209	2.43	2.03
Fe$_2$C	9.43	9.62	0.275	0.050	311	268	1.76	1.58
Fe$_7$C$_3$	8.71	9.10	0.099	0.052	365	229	1.91	1.72
Fe$_5$C$_2$	8.90	9.24	0.068	0.047	275	294	1.94	1.68
B1	8.00	7.96	0.754	0.597	501	334	0.00	0.00
B2	7.30	7.49	0.868	0.936	506	358	0.00	0.00
B3	10.00	9.62	1.289	0.475	542	254	0.00	0.00
ReO$_3$	12.90	12.44	0.974	0.837	255	205	0.00	0.00

our TB method is fit to cementite but gives an energy of around 100–200 meV higher for each of these other structures.

In examining Fe$_3$N we see that it is destabilized due to the lack of carbon-carbon bonding when compared with cementite. C-C distances are around 3.46 Å, near the end of the cutoff function, diminishing bonding interactions while repulsive interactions remain. Attempts to increase the bonding cutoff revealed that bonding is already low at this distance whether it is cut off or not. Thus, our repulsive term, which is fit to obtain the correct cementite formation energy, destabilizes these carbides. In another instance, Fe$_{23}$C$_6$, C-C bonds occur at 3.12 Å. As shown in the table, this structure is also destabilized, but not to the extent found in Fe$_3$N, reflecting the diminishing nature of the bond integrals. While bonding could be increased or repulsion decreased at larger distances in order to lower the energy of Fe$_3$N and other carbides, this results in the stabilization of the B2 structure. This ordered structure has not been observed, and its stabilization would cause significant problems in calculations within this model. However, despite these limitations, we obtain reasonable properties for B1 and B2, including lattice constant agreement and energies. The B3 (zinc blende) structure has a high energy in our model due to strong repulsive interactions, but TB calculations of the Fe-C dimer with our model gives both reasonable bonding energy, −4.17 eV in DFT versus −4.07 eV in TB, and equilibrium bonding distance, 1.56 Å in DFT versus and 1.67 Å in TB.

The magnetic moments on the Fe atoms are systematically higher by around 0.2 μ_B above DFT. This is inherited from the iron model (see Ref. [25]) as the magnetic moment in α Fe was overestimated by around 0.4 μ_B. This model does, however, capture the magnetic ordering in all of the carbides studied.

Given the importance of cementite in steel, we highlight our results in comparison with DFT. The TB calculated volume of cementite is 2.7% smaller than that found with DFT, and the formation energy is fit to match DFT. As the C-C repulsive interaction was fit to cementite, it is not surprising that the agreement with DFT is better than for other carbide structures. Finally, the magnetic moment per Fe atom is only 0.2 μ_B above DFT, in line with other carbide calculations. The TB bulk modulus in Table IV is in excellent agreement with DFT only 7 GPa above the DFT value.

Furthermore, we have calculated the individual elastic constants for cementite and report them in Table V. Here we see excellent agreement with previously published DFT results (see Ref. [7]). While C_{22} is reduced in TB by over 100 GPa, each of the other elastic constants agree with DFT to within 10 s of GPas. Most interestingly, we are able to reproduce the low C_{44} elastic constant that was a focus of the study.[7] This shows that our TB model is able to accurately describe even small intricacies of the elasticity of cementite. This confirms that the present TB model will give an accurate response to elastic distortions when in a stressed state.

C. Carbon and vacancy defects in iron

Beyond the description of carbides, the primary focus of this model is the calculation of carbon defects in iron. While a number of DFT studies have been performed on light elements in iron as outlined in the Introduction, here we compare a number of defect binding energies. This includes carbon-carbon and carbon-vacancy interactions with a variety of defect placements which will be used as another test of the TB model. No additional fitting is performed.

We look at defect binding energies using the formalism and test cases of Ref. [3], which were used to test an EAM potential for carbon in Fe. The binding energy (E_B) of a number of defects (e.g., A_1, A_2, A_3, etc.) may be expressed as

$$E_B(A_1, A_2, \ldots, A_n) = E(A_1 + A_2 + \cdots + A_n)$$
$$- \left[\sum_{i=1,\ldots,n} E(A_i) - (n-1)E_{ref} \right], \tag{7}$$

TABLE V. Elastic constants for cementite. DFT results taken from Ref. [7].

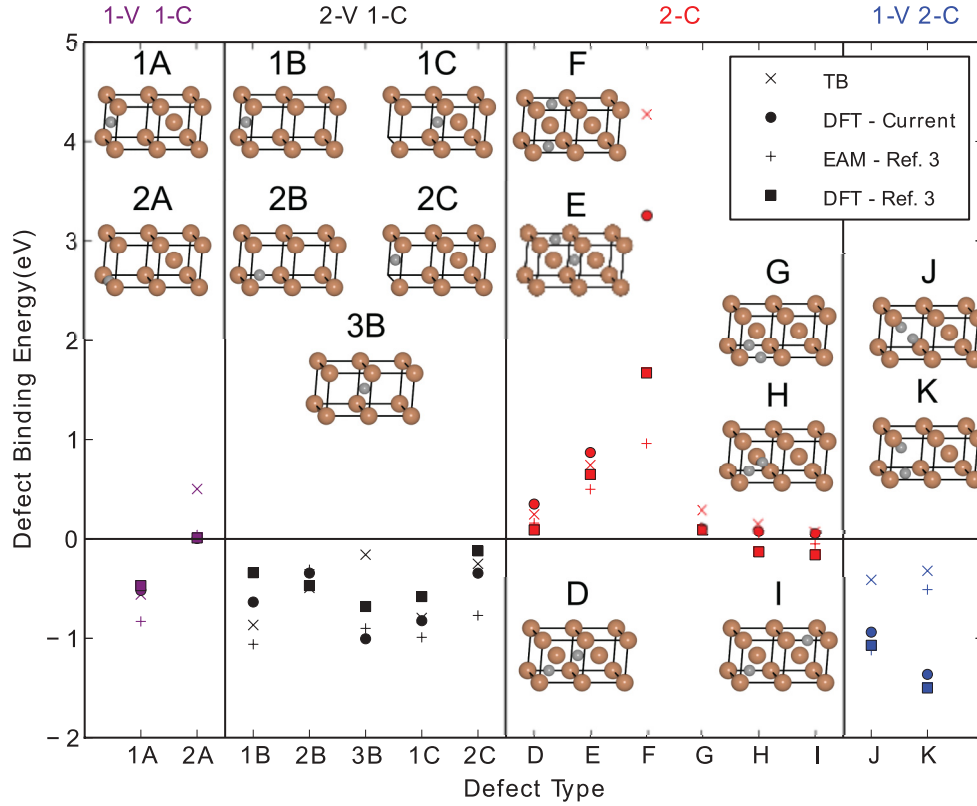|	C_{11}	C_{12}	C_{13}	C_{22}	C_{23}	C_{33}	C_{44}	C_{55}	C_{66}
DFT	388	156	164	345	162	322	15	134	134
TB	392	110	172	230	148	345	22	132	125

FIG. 9. (Color online) Defect energies of several different structures for DFT and TB methods with atomic relaxation employed. ×'s are TB and dots are DFT. Colors correspond to defect types: purple, one vacancy and one carbon; black, two vacancies and one carbon; red, two carbons; and blue, two carbons and one vacancy. Current calculations were performed in a 54 iron-atom supercell of FM α iron (bcc). Comparisons with EAM and DFT are taken from Ref. 3.

where $E(A_1 + A_2 + \cdots + A_n)$ is the energy of a cell containing numerous defects, $E(A_i)$ is the energy of a cell containing a single defect, and E_{ref} is the energy of the defect-free supercell. Defect groups with an attractive interaction will have a negative E_B. We calculate the binding energy of defects and vacancies in a $3 \times 3 \times 3$ supercell of magnetic α iron (54 iron atoms) and compare them with present VASP calculations. These are shown in Fig. 9. Our plane-wave cutoff for VASP calculations (500 eV) is higher than used previously (290 eV). We use a system size of 54 iron atoms throughout as opposed to the mixed configuration of both 54 and 128 iron atoms used previously. Despite these differences, we achieved good agreement with the previous DFT calculations with a few exceptions that are noted below, and we performed TB calculations with 128 atoms to check any discrepancies. We also note differences with the EAM potential of Ref. 3.

For the one vacancy and one carbon calculations, we obtain good agreement for 1A and qualitatively agree for both cases; 1A is attractive, 2A is repulsive. 2A, however, is too repulsive when compared to DFT. In contrast, the EAM potential shows better agreement for 2A but overestimates the attractive binding of 1A. When an additional vacancy is added in cases B and C, we find good quantitative agreement within 200 meV for all interactions except 3B. Qualitatively, all interactions are attractive, and we find overall agreement that compares favorably with the EAM potential.

The TB model of the two carbon defects gives very good agreement with DFT both quantitatively and qualitatively.

Compared to the previous 128 iron-atom calculations, we obtain a more repulsive interaction for configuration F, likely due to our smaller supercell, of 4.27 eV with TB and 3.25 eV with DFT. By enlarging our cell size to 128 iron atoms, the repulsion is reduced to 1.80 eV with TB and 1.82 eV with the present DFT calculations as compared to the reported DFT and EAM values of 1.67 and 0.96 eV, respectively. Thus, the TB model obtains closer agreement with DFT in this instance than the EAM. The H and I setups of Ref. 3 are reported as slightly attractive, whereas we find them to be slightly repulsive for both TB and DFT. In this case, while an increase in system size to 128 iron atoms does lower the interaction between the carbon atoms, we obtain DFT values of within 20 meV of 0 eV, with I being the only slightly attractive interaction. Our TB results show slight repulsion for both 54 and 128 iron-atom cells.

Last, we examine defect configurations J and K which are composed of one vacancy and two carbon interstitials. This configuration requires an accurate portrayal of C-C bonding in the model due to the proximity of the carbons and the presence of a vacancy which reduces iron screening. In K a dimer is formed as the carbons coalesce in both DFT and TB, while there is only a short contraction of the C-C distance in J. We calculate similar C-C distances in each method, but DFT has a more attractive C-C interaction as seen in the differences of the dimer total energies in Fig. 5. The ordering of the binding energies is not reproduced (as is the case for the EAM potential), but the attraction of the defects is correctly calculated by TB in each instance.

One likely limitation of the TB model could be due to a poor description of the vacancy energy in the Fe model. This was explained in Ref. 25 and may account for some of the differences in 2A, 3B, J, and K. We note that this model was constructed to be extremely simple, using only two fitting parameters for the Fe-C interaction and an additional C-C repulsive fitting parameter. Despite this, and despite the fact that the DFT energies reported here vary by up to 400 meV from the previous DFT study, these results illustrate the versatility of this TB model for calculating a range of defect states. Furthermore, while the results in this section are for α iron, this TB model should be applicable to fcc and hcp iron as well, giving it the flexibility to tackle problems that EAM potentials cannot.

IV. DISCUSSION AND CONCLUSIONS

The purpose of constructing parameterized models lies in the need for extending the range of electronic structure calculations. Here, we have constructed a parametrized method for the calculation of the electronic structure of carbon in iron. We accomplish this with an orthogonal pd model using local charge neutrality. Bonding is extracted directly from DFT calculations via a downfolding procedure to obtain a two center parametrization of the bond integrals. Fitting remaining exponential repulsive terms to excess energies of carbon in iron with only three adjustable parameters gives a model that can make predictions for a number of questions in steel research.

The electronic structures of cementite, ordered iron carbides, and carbon in bcc iron are well reproduced with slight differences in the bandwidth. The behavior of bonding via p and d states is retained. Thus, insights about electronic structure and bonding may continue to be drawn from this simplified model. We are able to obtain the correct ordering of energies of the carbon-only structures in this model, albeit with the incorrect energies and lattice constants. Thus, our model is limited to iron-rich structures and would have difficulties calculating, for example, the correct energy of graphite layers within iron, as it suppresses graphite formation.

The model is tested by calculating the formation energies, lattice constants, bulk moduli, and magnetic properties of a number of carbides in comparison with DFT. The properties of cementite and other carbides are reasonable in agreement with DFT. The individual elastic constants of cementite are especially noteworthy, as they are in excellent agreement with previous DFT studies and show a small C_{44} value. No carbides are overstabilized with respect to cementite. This allows the model to be employed when studying cementite in the presence of interfaces with iron and other phenomena. Additionally, there is excellent agreement with magnetic properties of the carbides captured by this model.

We calculated a range of carbon defects in iron. We obtain a realistic migration barrier of 0.70 eV and confirm that carbon is unstable in the tetrahedral interstitial site via NEB calculations. For the range of defect calculations previously calculated by Becquart *et al.*,[3] we obtain qualitative and quantitative agreement with DFT, in several instances better than previous EAM potentials. As an outlook, this model is ideally suited for performing these same calculations in fcc and hcp iron, making it a much more versatile method than possible with EAM potentials.

Thus, this is a foundation for continuing work on light elements in steel. By establishing a clear process for TB model development, the calculation of multicomponent and complex alloys in steel is possible. Additionally, this method may be coarse grained into BOPs to increase its system size, accommodating the calculation of millions of atoms, as has been shown for iron.[38] Moreover, by creating a simplified picture of bond formation and magnetism, our model possesses the ability to divine mechanisms and origins of material behavior, thus providing solutions for steel design.

[1] D. E. Jiang and E. A. Carter, Phys. Rev. B **67**, 214103 (2003).

[2] C. Domain, C. S. Becquart, and J. Foct, Phys. Rev. B **69**, 144112 (2004).

[3] C. S. Becquart, J. M. Raulot, G. Bencteux, C. Domain, M. Perez, S. Garruchet, and H. Nguyen, Comput. Mater. Sci. **40**, 119 (2007).

[4] S. V. Okatov, A. R. Kuznetsov, Y. N. Gornostyrev, V. N. Urtsev, and M. I. Katsnelson, Phys. Rev. B **79**, 094111 (2009).

[5] D. W. Boukhvalov, Y. N. Gornostyrev, M. I. Katsnelson, and A. I. Lichtenstein, Phys. Rev. Lett. **99**, 247205 (2007).

[6] E. Hristova, R. Janisch, R. Drautz, and A. Hartmaier, Comput. Mater. Sci. **50**, 1088 (2011).

[7] C. Jiang, S. G. Srinivasan, A. Caro, and S. A. Maloy, J. Appl. Phys. **103**, 043502 (2008).

[8] V. I. Voronin, I. F. Berger, Y. N. Gornostyrev, V. N. Urtsev, A. R. Kuznetsov, and A. V. Shmakov, JETP Lett. **91**, 143 (2010).

[9] A. Dick, F. Kormann, T. Hickel, and J. Neugebauer, Phys. Rev. B **84**, 125101 (2011).

[10] H. Faraoun, Y. Zhang, C. Esling, and H. Aourag, J. Appl. Phys. **99**, 093508 (2006).

[11] C. M. Fang, M. A. van Huis, and H. W. Zandbergen, Phys. Rev. B **80**, 224108 (2009).

[12] K. O. E. Henriksson, N. Sandberg, and J. Wallenius, Appl. Phys. Lett. **93**, 191912 (2008).

[13] C. M. Fang, M. A. Van Huis, M. H. F. Sluiter, and H. W. Zandbergen, Acta Mater. **58**, 2968 (2010).

[14] C. M. Fang, M. A. van Huis, J. Jansen, and H. W. Zandbergen, Phys. Rev. B **84**, 094102 (2011).

[15] M. S. Daw and M. I. Baskes, Phys. Rev. B **29**, 6443 (1984).

[16] T. T. Lau, C. J. Forst, X. Lin, J. D. Gale, S. Yip, and K. J. Van Vliet, Phys. Rev. Lett. **98**, 215501 (2007).

[17] D. J. Hepburn and G. J. Ackland, Phys. Rev. B **78**, 165115 (2008).

[18] M. Ruda, D. Farkas, and G. Garcia, Comput. Mater. Sci. **45**, 550 (2009).

[19] R. Drautz and D. G. Pettifor, Phys. Rev. B **74**, 174117 (2006).

[20] D. G. Pettifor, Phys. Rev. Lett. **63**, 2480 (1989).

[21] M. W. Finnis, Prog. Mater. Sci. **52**, 133 (2007).

[22] R. Drautz and D. G. Pettifor, Phys. Rev. B **84**, 214114 (2011).

[23] H. Amara, J. M. Roussel, C. Bichara, J. P. Gaspard, and F. Ducastelle, Phys. Rev. B **79**, 014109 (2009).

[24] E. R. Margine, A. N. Kolmogorov, M. Reese, M. Mrovec, C. Elsasser, B. Meyer, R. Drautz, and D. G. Pettifor, Phys. Rev. B **84**, 155120 (2011).

[25] G. K. H. Madsen, E. J. McEniry, and R. Drautz, Phys. Rev. B **83**, 184119 (2011).

[26] E. J. McEniry, G. K. H. Madsen, J. F. Drain, and R. Drautz, J. Phys.: Condens. Matter **23**, 276004 (2011).

[27] A. P. Sutton, M. W. Finnis, D. G. Pettifor, and Y. Ohta, J. Phys. C **21**, 35 (1988).

[28] J. Slater and G. Koster, Phys. Rev. **94**, 1498 (1954).

[29] J. Enkovaara, C. Rostgaard, J. J. Mortensen, J. Chen, M. Dułak, L. Ferrighi, J. Gavnholt, C. Glinsvad, V. Haikola, H. A. Hansen *et al.*, J. Phys.: Condens. Matter **22**, 253202 (2010).

[30] A. H. Larsen, M. Vanin, J. J. Mortensen, K. S. Thygesen, and K. W. Jacobsen, Phys. Rev. B **80**, 195112 (2009).

[31] A. Urban, M. Reese, M. Mrovec, C. Elsasser, and B. Meyer, Phys. Rev. B **84**, 155119 (2011).

[32] S. Satpathy, V. P. Antropov, O. K. Andersen, O. Jepsen, O. Gunnarsson, and A. I. Liechtenstein, Phys. Rev. B **46**, 1773 (1992).

[33] G. Kresse and J. Hafner, Phys. Rev. B **48**, 13115 (1993).

[34] G. Kresse and J. Furthmüller, Phys. Rev. B **54**, 11169 (1996).

[35] G. Kresse and J. Furthmüller, Comput. Mater. Sci. **6**, 15 (1996).

[36] P. E. Blöchl, Phys. Rev. B **50**, 17953 (1994).

[37] G. Kresse and D. Joubert, Phys. Rev. B **59**, 1758 (1999).

[38] M. Mrovec, D. Nguyen-Manh, C. Elsasser, and P. Gumbsch, Phys. Rev. Lett. **106**, 246402 (2011).